Force generation due to three-dimensional plasma discharge on a conical forebody using pulsed direct current actuators

Kunwar Pal Singh and Subrata Roy[a)]
Computational Plasma Dynamics Laboratory and Test Facility, Department of Mechanical and Aerospace Engineering, University of Florida, Gainesville, Florida 32611, USA

(Received 3 January 2008; accepted 14 March 2008; published online 20 May 2008)

Understanding the behavior of three-dimensional plasmas around a pulsed dc actuator can be useful for its efficient operation in many applications. The effect of such actuators is studied using a self-consistent multibody system of neutral oxygen species and its plasma. The equations governing the motion of charged species are solved with the drift diffusion approximation. The electrostatic potential is computed from Poisson's equation. The electric field and ionization level are the highest close to the junction of electrodes and dielectric. The plasma body force thus generated also follows a similar characteristic. Results also show some dc corona instabilities. The temporal average of such force shows mostly acceleration from anode to cathode above the actuator. © *2008 American Institute of Physics*. [DOI: 10.1063/1.2924422]

I. INTRODUCTION

Reported experiments and numerical predictions[1–9] show that plasma actuators have the ability to impart body force inside the boundary layer of a fluid in the vicinity of a surface. Such force successfully controlled flow separation on airfoils at a high angle-of-attack, increased the lift, and/or reduced the drag of airfoils and fuselages. It is important to identify the three-dimensional effect, if any, of force generation due to an operational plasma actuator. To our knowledge, the reported numerical efforts are either one- or two-dimensional, and the experimental efforts lack temporally and spatially resolved data.

The plasma in actuators may operate under a Townsend avalanche and a glow discharge. The V-dot probe technique shows that the voltage across the plasma is less than half of that which is applied across the electrodes[10] in a large vacuum chamber and a linear relationship between the force production and air pressure was found during experimental measurements of the force of a plasma actuator.[11] The airflow was found to have a significant influence on the plasma characteristics during an investigation of different airflow velocities, plasma excitation frequencies, and voltages.[12] The body force was found to be proportional to frequency for a constant voltage. The body force increases with voltage for a constant frequency.[13] The induced jet velocity depends on the applied voltage and frequency.[14,15] The actuator power can be reduced by 90% and its durability can be improved by operating it in an unsteady manner.[16]

The plasma actuator was also treated with heat and momentum input into a small control volume.[2] Reported measurements indicate that the momentum coupling between the charged particles and the neutral particles occurs on timescales much shorter than that for the bulk fluid motion. The description of the plasma-fluid interaction involves interplay between electron, ion and fluid timescales. The electron plasma frequency is $\sim 10^9$ Hz, the ion plasma frequency is $\sim 10^6$ Hz, and that of the fluid (speed/domain) frequency is $\sim 10^3$ Hz. As the speed increases, for example, with Mach number, the flow frequency increases and at very high speeds the ion plasma frequency may become comparable to the flow frequency. At hypersonic flows nonequilibrium chemical kinetics will also affect the energy transfer mechanisms. Another mode of momentum coupling can be achieved using wall temperature injection influencing the thermal boundary layer through electrical or other means. Theoretical details of such coupling will be discussed in a future paper.

A detailed numerical model of plasma with eight species air chemistry with nitrogen and oxygen mixture by the authors has found the effect of different charged species into the generation of electrodynamic force that controls the flow of the surrounding fluid.[6] However, the influence of plasma actuators are limited by different kinds of power losses such as reactive power losses due to impedance mismatch between the power supply and the actuator, dielectric heating, and plasma Joule heating which need to be minimized for optimum performance.[17,18]

As a specific application, flight vehicle forebody vortex symmetry breaking and control of resulting yaw departure by active and passive means have been studied by many researchers. Such study includes numerical simulation, analytical interpretation, and experiments.[19–25] For example, flow control using flow injection and surface heating has been investigated for asymmetric flows around circular cones by using a computational solution of the unsteady, compressible full Navier–Stokes equations.[19] Various computational aspects of two-dimensional modeling are extensively discussed in Ref. 20. Passive vortical flow control on a wing-body combination using tangential blowing has also been studied.[21] The feasibility of using forebody tangential blowing to control the roll-yaw motion of a wind-tunnel model at high angles of attack has been shown experimentally.[22] Analytical modeling for a circular cone for determining the sta-

[a)]Author to whom correspondence should be addressed. Electronic mail: roy@ufl.edu.

bility of point vortices to small symmetric and asymmetric displacements was qualitatively validated against experimental results.[23]

As an alternative to blowing, surface discharge plasmas may be employed to actively control or eliminate vortical asymmetry about the nose of a conical forebody at an angle of incidence. High-frequency spark discharge plasma was used to control asymmetric vortical structures on the conical forebody.[24] Results of wind-tunnel experiments show that plasma actuators distributed near flow separation lines may be used for successful control or elimination of vortex asymmetry. A two-dimensional theoretical study for flow control over a conical section was reported using a single barrier discharge actuator and a set of dc plasma actuators.[25] Results show insufficient control of the flow on the entire length of the forebody due to a single barrier discharge actuator. Flow control on the conical forebody cross-section using several pulsed dc plasma actuators show considerable improvement for separated neutral gas flow at 17.5° angle-of-attack. In general, two-dimensional details are limited in exploring discharge constrictions and instability structures, and thus the three-dimensional analysis of force generation mechanism remains necessary.

As an extension of our two-dimensional model,[3,6,25] in this paper we present the results of the flow control on a three-dimensional conical forebody using pulsed dc plasma actuator operating in weakly ionized oxygen gas. Section II gives details of oxygen chemistry. Section III provides details of the computational geometry, initial and boundary conditions and numerical details. The response to the applied pulsed dc potential is described in Sec. IV. Conclusions are drawn in Sec. V.

II. OXYGEN CHEMISTRY

For the oxygen chemistry we neglect the metastable species along with O^{4+} due to their extremely high recombination rates. O_2^- is not included in this paper due to the reason explained at the end of Sec. IV. Also, the numerical complexity is further simplified by excluding nitrogen chemistry at this stage. The model equations governing the chemistry of discharge are as follows.[26]

(a) ionization $e + O_2 \rightarrow O_2^+ + 2e$, (1a)

(b) dissociation $e + O_2 \rightarrow 2O + e$, (1b)

(c) dissociative attachment $e + O_2 \rightarrow O_- + O$, (1c)

(d) recombination $O^- + O_2^+ \rightarrow O + O_2$, (1d)

(e) dissociative recombination $O + O^- \rightarrow O_2 + e$, (1e)

The drift-diffusion form of continuity and Poisson equations for the electrons, ions, and neutrals are as follows:

$$\frac{\partial n_e}{\partial t} + \nabla \cdot (n_e \mathbf{v}_e) = (k_1 - k_3) n_e n_{O_2} + k_5 n_O n_{O^-}, \quad (2)$$

$$\frac{\partial n_{O_2}}{\partial t} + \nabla \cdot (n_{O_2} \mathbf{v}_{O_2}) = -(k_1 + k_2 + k_3) n_{O_2} n_e + k_4 n_{O^-} n_{O_2^+} + k_5 n_O n_{O^-}, \quad (3)$$

$$\frac{\partial n_O}{\partial t} + \nabla \cdot (n_O \mathbf{v}_O) = (2k_2 + k_3) n_e n_{O_2} + k_4 n_{O^-} n_{O_2^+} - k_5 n_O n_{O^-} \quad (4)$$

$$\frac{\partial n_{O^-}}{\partial t} + \nabla \cdot (n_{O^-} \mathbf{v}_{O^-}) = k_3 n_e n_{O_2} - k_4 n_{O^-} n_{O_2^+} - k_5 n_O n_{O^-}, \quad (5)$$

$$\frac{\partial n_{O_2^+}}{\partial t} + \nabla \cdot (n_{O_2^+} \mathbf{v}_{O_2^+}) = k_1 n_e n_{O_2} - k_4 n_{O^-} n_{O_2^+}, \quad (6)$$

$$\nabla \cdot (\varepsilon \nabla \phi) = 4\pi e (n_e + n_{O^-} - n_{O_2^+}), \quad (7)$$

with momentum flux

with momentum flux $n_\alpha \mathbf{v}_\alpha$

$$= -\operatorname{sgn}(e) n_\alpha \mu_\alpha \nabla \phi - D_\alpha \nabla n_\alpha, \quad (8)$$

and electric field $\mathbf{E} = -\nabla \phi$. (9)

The electron temperature is calculated from $\mathbf{E} = k_B T_e / (\nabla n_e / n_e)$, which is obtained assuming an initial Boltzmann distribution $n_e \propto \exp(e\phi / k_B T_e)$. Various rate coefficients $k_1, k_2, \ldots, k_5$ related to in Eqs. (1a)–(1e) are obtained[26] as functions of electron temperature. The secondary electron emission from the exposed surface is taken as a function of incident electron energy[27] and remains small, i.e., less than 10^{-3}. No material sputtering of the surface is considered. In Eqs. (2)–(9), n_α and $\mathbf{v}_\alpha$ are the density and velocities of species α, respectively. The mobilities μ_α and diffusion rates D_α are given.[28] The bulk density of the oxygen is taken to be 0.35 kg/m^3 at atmospheric pressure.

III. NUMERICAL MODEL

Figure 1 shows the schematic of a pulsed dc plasma actuator. The simulated region is 60° segment of a cone. The segment extents from $z=0.06$ cm to $z=4.0$ cm. The surface containing the electrodes and dielectric is given by $x = 0.16 \sin(360-\alpha)$ cm to $x = 0.5 \sin(360-\alpha)$ cm and $y = 0.16 \cos(360-\alpha)$ cm to $y = 0.5 \cos(360-\alpha)$ cm, where α varies from 0° to 60°. The domain of simulation consists of a 2 mm thick air packet coating over this curved surface. The domain size is sufficient to capture the physics of plasma dynamics. We study only plasma dynamics in the present work. The present domain size is not sufficient to capture dynamics of the air flow (for Navier–Stokes equations) which needs a bigger domain size. The pulsed dc plasma actuator consists of four electrodes separated by a dielectric. The powered electrodes are marked by P and grounded electrodes by G in Fig. 1. The electrodes are exposed to the air. The thickness of each electrode is 2.0 mm along the z-direction. The powered and grounded electrodes are separated by a dielectric. The thickness of dielectric separating the electrodes is 2.0 mm along the z-direction. The powered

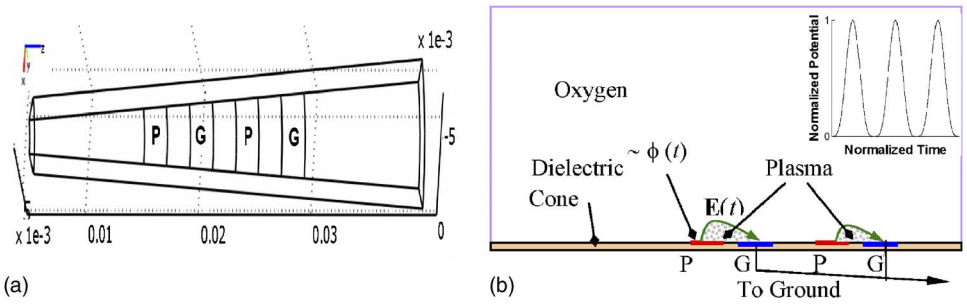

FIG. 1. (Color online) Schematic of three-dimensional plasma discharge on a conical forebody using pulsed dc actuators operating in oxygen gas. The simulated region is 60° segment of a cone. The segment extents from $z=0.06$ cm to $z=4.0$ cm. The surface containing the electrodes and dielectric is given by $x=0.16\sin(360-\alpha)$ cm to $x=0.5\sin(360-\alpha)$ cm and $y=0.16\cos(360-\alpha)$ cm to $y=0.5\cos(360-\alpha)$ cm, where α varies from 0° to 60°. The domain of simulation consists of a 2 mm thick air packet coating over this curved surface.

electrodes are from $z=1.6$ cm to $z=1.8$ cm and from $z=2.4$ cm to $z=2.6$ cm. The dielectric surface between the electrodes is from $z=1.8$ cm to $z=2.0$ cm, from $z=2.2$ cm to $z=2.4$ cm, and from $z=2.6$ cm to $z=2.8$ cm. The grounded electrode is from with $z=2.0$ cm to $z=2.2$ cm and from $z=2.8$ cm to $z=3.0$ cm. We have chosen the relative dielectric constant $\varepsilon_r=10$. The domain is filled with air of relative dielectric constant $\varepsilon_r=1.0055$. The height of the electrodes is assumed negligible. A pulsed dc voltage of $\phi=\phi_0\sin^4(2\pi ft)$ volts is applied to the powered electrode. Such pulsed dc voltage can be produced by commercially available function generators and can be amplified. We have chosen with $\phi_0=1000$ V and $f=5$ kHz.

Initial conditions are as follows: The all initial particle concentrations, except those of the electrons, and oxygen molecules, are taken to be zero. The initial atmospheric oxygen molecule density is taken as $10^{26}/\mathrm{m}^3$, and the electron density is taken as $10^9/\mathrm{m}^3$. The initial pulsed dc potential is zero. These initial conditions have been chosen to match with the realistic atmospheric conditions.

The boundary conditions for Poisson's equation are as follows: The potential difference with $\phi_0=1000$ V is applied to the first electrode of the pair. The other electrode of the pair is grounded. The powered electrodes are marked by **P** and grounded electrodes by **G** in Fig. 1. The powered and grounded electrodes are separated by a dielectric. An electric insulation condition (normal component of electric field equal to zero) is assumed at outer boundaries of the domain and at the dielectric surface.

Boundary conditions related to oxygen species continuity equations are as follows: The currents flow normal only to the rf electrode since it is an equipotential surface. Homogeneous Neumann conditions are applied to the outer edges of the domain and electric insulation is assumed at the surface of the dielectric. The normal currents at the surface of dielectric are taken to be zero.

The ionized oxygen gas is numerically modeled using a self-consistent three-dimensional Galerkin variational formulation based finite element method to obtain electron, ion, and neutral species densities of oxygen and the electric potential distribution. Finite element techniques[3,4,14,17,25] are well known for their adaptability to arbitrary multidimensional geometries and accurate imposition of complicated boundary conditions. Here, the equation sets [Eqs. (1)–(9)] can be written with operator L as $\mathrm{L}(\mathbf{U})=0$ where **U** contains state variables such as species number densities and potential. Multiplying with a permissible test function η and integrating over the spatially discretized domain Ω, the variational statement results in the following weak form:

$$WS^h=\Im_e\left(\int_{\Omega_e}[\eta L(\mathbf{U})d\tau]\right)=0, \tag{10}$$

for a discretization h of $\Omega=\cup\Omega_e$ and $\Im_e$ is the nonoverlapping sum over the elements. The application of Green–Gauss divergence theorem "weakens" the order of derivatives in Eq. (10) and yields natural homogenous Neumann boundary conditions. The surface integral thus resulting in Eq. (10) contains the (un)known boundary fluxes wherever fixed or flux boundary conditions are enforced accurately. Thus, for example, the Galerkin form of Eq. (7) becomes

$$\sum_e\left(\int_{\Omega_e}\frac{d\eta}{dz}\varepsilon\frac{d\eta^T}{dz}dz\{\phi\}_e+e\int_{\Omega_e}\eta\eta^T dz\{n_e\}_e-e\int_{\Omega_e}\eta\eta^T dz\{n_{O_2^+}\}_e+e\int_{\Omega_e}\eta\eta^T dz\{n_{O^-}\}_e-\int_{\Omega_e\cap\partial\Omega_e}\eta\varepsilon\frac{d\eta^T}{dz}dz\{\phi\}_e=F_\phi\right)_e, \tag{11}$$

where F_ϕ is the solution residual.

The Jacobian matrix $J=[\partial F/\partial\mathbf{U}]$ in the global $[J].\{\partial\mathbf{U}\}=-\{F\}$ is resolved using the LU- decomposition scheme for updating change in discretized solution vector **U** at each iteration. The terminal nonlinear ordinary differential equation (ODE) systems are solved using implicit Euler method for temporal evolution and NR iterative algorithm for the nonlinear matrix algebra. The convergence criterion for all variables at any iteration is set at 10^{-4}. Solution stability is ensured by appropriate selection of adaptive time marching step size (with the smallest step of one hundredth of the dielectric relaxation timescale) and the introduction of artificial diffusion. The number of degrees of freedom employed is 123 816.

Independent of the physical dimension of the working domain Ω, and for general forms of the flux vectors, the semidiscretized weak statement always yields an ODE system that is *fully discretized* using a θ-implicit or τ-step Runge–Kutta type time integration. The terminal ODE is usually solved using a Newton–Raphson scheme for $\mathbf{U}(t)$,

$$\mathbf{U}_{\tau+1}^{i+1} = \mathbf{U}_{\tau+1}^{i} + \Delta\mathbf{U}^{i} = \mathbf{U}_{\tau} + \sum_{p=0}^{i} \mathbf{U}^{p+1},$$

where

$$\Delta\mathbf{U}^{i} = -[\mathbf{M} + \theta\Delta t(\partial\mathbf{R}/\partial\mathbf{U})]^{-1}\mathbf{R}(\mathbf{U}). \quad (12)$$

Here, a θ-implicit time marching procedure is employed. In Eq. (12), $\mathbf{M}=S_e(\mathbf{M}_e)$ is the "mass" matrix associated with element level interpolation, and $\mathbf{R}$ carries the element convection, diffusion, and source information. The calculation of the "Jacobian" $\partial\mathbf{R}/\partial\mathbf{U}$ and inversion of the $\mathbf{M}+\theta\Delta t(\partial\mathbf{R}/\partial\mathbf{U})$ matrix with sufficient accuracy is obviously a numerical challenge. However, unlike the traditional finite difference/volume methods, the present finite element (FE) algorithm allows one to simulate the system simultaneously without requiring any subiteration for the Poisson solver.

In order to resolve the plasma details in three-dimensions it is crucial to resolve the wall sheath region. So, we used the smallest element thickness of the order of Debye length around the powered electrode. The mesh density was proportional to the electric field intensity in all three-directions. Note in this case that we are not attempting to calculate the fluid flow which would require a very large domain with submillimeter scale flow mesh to be overlapped on the micron scale plasma mesh. In such case, in three-dimensions several hundreds of millions of degrees of freedoms will be solved mandating some multilevel parallel coding approach and weeks of simulation time to cover all timescales. The level of computational challenge will even increase further as we include more complexity of finite rate air chemistry with large species array. We contain such challenges by solving drift-diffusion approximated plasmas incorporating only electron and four species of oxygen gas.

IV. RESULTS AND DISCUSSION

Discharge starts in the oxygen as we switch on the pulsed dc voltage. Different ion and neutral species are formed through ionization, dissociation, and dissociative attachment, etc. Recombination also occurs. The full chemistry of different species formation and recombination is described by Eq. (1). The simulation results at the peak of the tenth cycle of the pulsed dc are given in Figs. 2–6.

Figures 2(a) and 2(b) show electric potential and electric field components as a function of z at $\alpha=15°$ and 45° for a pulsed dc plasma actuator. As mentioned earlier that very first electrode from the left is the powered electrode. Then there is dielectric of 2 mm thickness and then a grounded electrode. The sequence is repeated for second set of electrodes and dielectric. The variation of various components of electric field on the surface follows from applied of electric potential. The electric field is given by $\mathbf{E}=-\nabla\phi$. Since the gradient of electric field is highest at the edges the electrodes, the value of electric field is highest there. The potential does not change with z for the powered and grounded electrodes. The gradient of the electric potential with respect to z is zero. The value of E_z is zero at the electrodes surfaces. The potential is not constant with respect to x or y, hence E_x and E_y are not zero at the electrode surfaces. The curvature

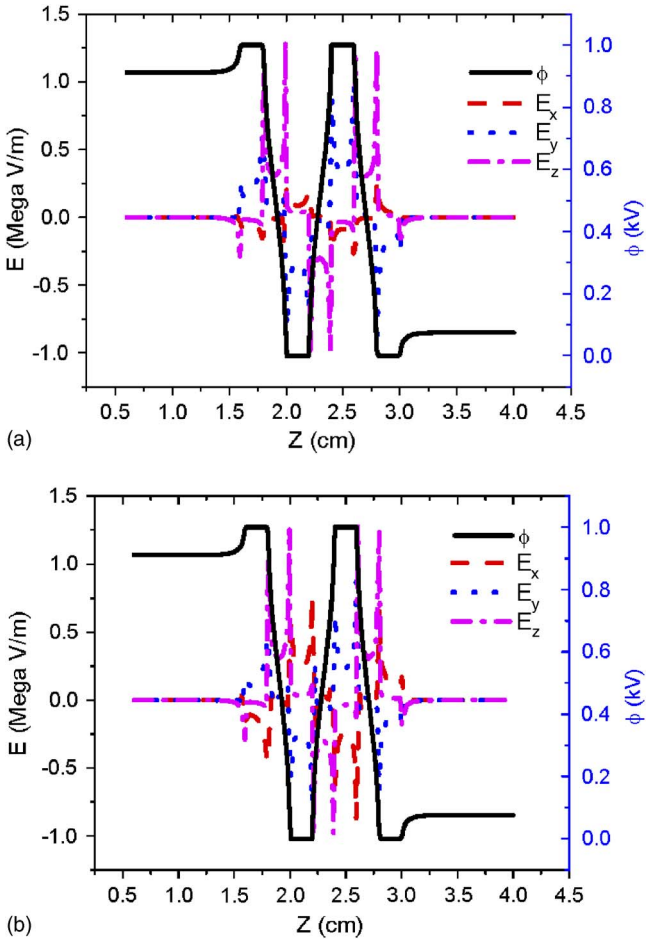

FIG. 2. (Color online) Electric potential and electric field components as a function of z at (a) $\alpha=15°$ and (b) $\alpha=45°$.

of the electrodes with lower values of z is high; the electric field is high for these electrodes. Higher ionization occurs for these electrodes.

Figure 3(a) shows the spatial distribution of electron density for the pulsed dc plasma actuator. The chemistry of electrons formation is given by set of Eq. (1a). Spatial and temporal density profiles of electrons are governed by the continuity equation [Eq. (2)] coupled with other equations. Electron density rises up to a level $4\times10^{14}/\mathrm{m}^3$. Electrons respond to the electric field very fast due to low mass and high mobility. The electrons are repelled from the area of grounded electrode and are attracted towards the rf electrode where they are lost. Figure 4(a) shows slices of density of electrons at the positive peak of the pulsed dc of tenth cycle. The density decreases sharply with the increase in the distance from the surface of the electrodes and dielectric.

The oxygen ions O^- are produced through dissociative attachment of oxygen molecules with electrons governed by the Eq. (1c). Its density is governed by the continuity equation [Eq. (5)] coupled with other equations. The density of oxygen ions O^- grows to a level of nearly $3\times10^{15}/\mathrm{m}^3$. Figure 3(b) shows the density profile of negative oxygen ions O^- at the positive peak of the pulsed dc of tenth cycle. The negative oxygen ions play an important role in oxygen chemistry. The oxygen ions O^- are repelled from the area of grounded electrode and are attracted towards powered elec-

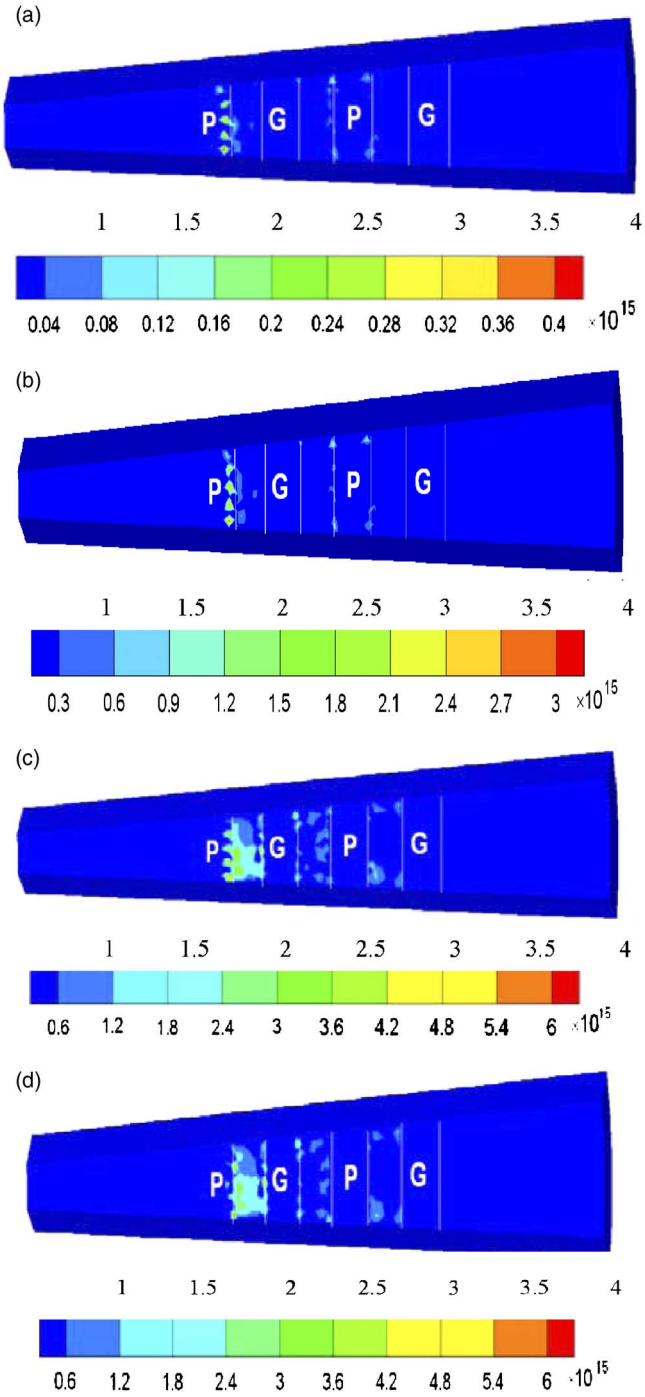

FIG. 3. (Color online) Surface plot of density (m^{-3}) of (a) electrons, (b) negative oxygen ions O^-, (c) positive oxygen ions O_2^+, and (d) charge separation $n_q = n_{O_2^+} - n_e - n_{O^-}$.

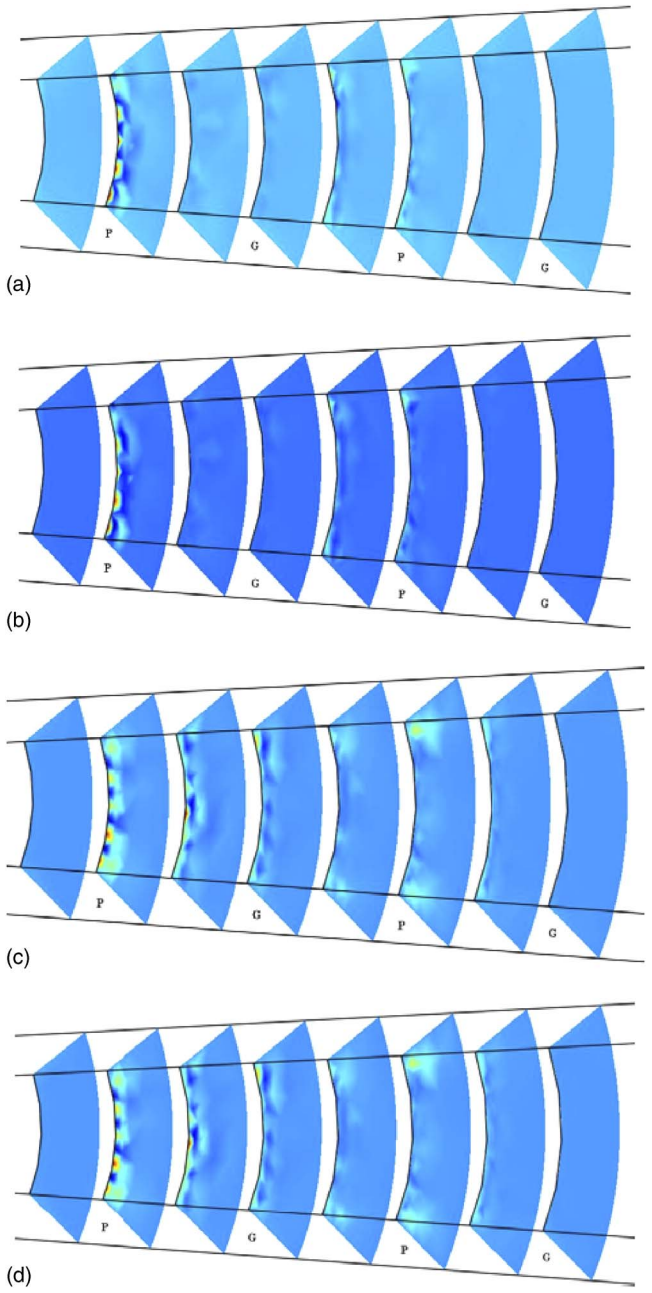

FIG. 4. (Color online) Slices of density (m^{-3}) of (a) electrons, (b) negative oxygen ions O^-, (c) positive oxygen ions O_2^+, and (d) charge separation $n_q = n_{O_2^+} - n_e - n_{O^-}$.

trode under the influence of pulsed dc. At the electrode oxygen ions O^- become a part of normal current. The oxygen ions O^- are much heavier than that of electrons and its mobility is low; the response is slow.

The edge of the powered electrode is at $z=1.8$ cm. The peak of density is close to the edge of the powered electrode. The electric field is highest at the edges hence higher ionization occurs at these locations. The curvature of the electrodes at lower values of z is higher. The electric field is higher for higher curvature. This increases ionization for the electrodes with lower values of z. Figure 4(b) shows slices of the density of negative oxygen ions O^- at the positive peak of the pulsed dc of the tenth cycle at electrode edges. The density decreases sharply with the increase in the distance from the edge of the electrodes or dielectric.

The response of negative species to the electric field is opposite to that of positive ions. Ion mass and motilities are also different for different oxygen species and electrons, hence, their velocities are different. This gives rise to charge separation given by $n_q = n_{O_2^+} - n_e - n_{O^-}$. Figure 3(d) shows the density profile of the charge separation at the positive peak of the tenth cycle. It resembles that of density profiles of positive oxygen ions. The densities of charge species such as electrons and O_2^- are small in comparison to O_2^+ ions. The value of charge separation q is nearly equal to density of O_2^+

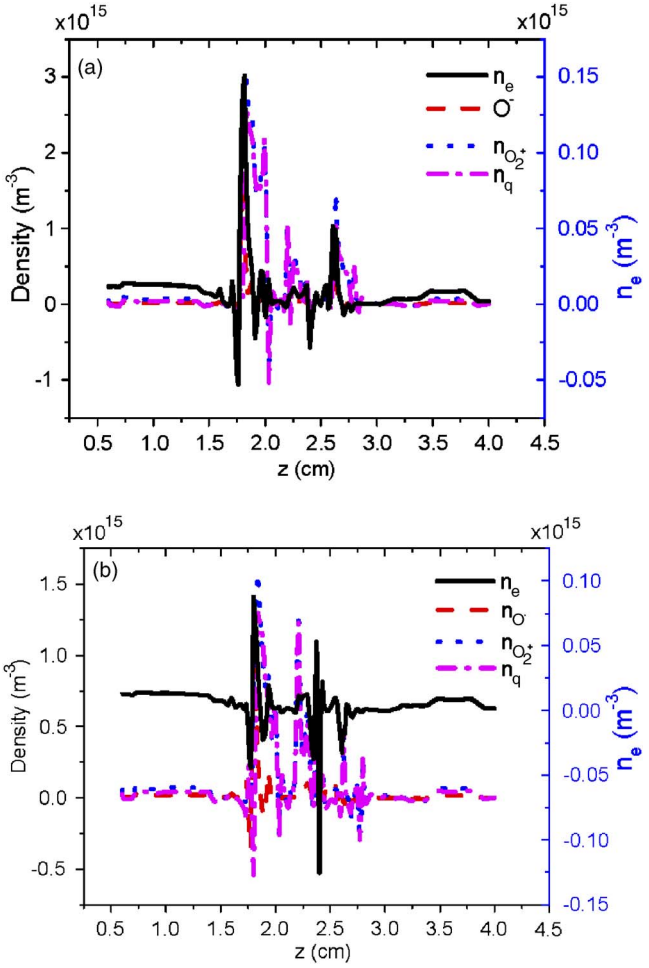

FIG. 5. (Color online) Density of various charge species at (a) $\alpha=15°$ and (b) $\alpha=45°$.

ions. Figure 4(d) shows slices of the density of charge separation at the edges of electrodes at the positive peak of the pulsed dc of the tenth cycle. The peak of charge separation is very close to the common edge of the powered electrode and dielectric. The strength and direction of the electric field and charge of various species are responsible for this location of densities. Charge separation gives rise to a self-generated electric field through Poisson's equation. The density decreases sharply with the increase in the distance from the edges of the electrodes or dielectric. The localized hotspots near the electrodes are similar to that seen in experiments and may be signatures of dc corona instability. Figures 5(a) and 5(b) show the density of various charge species at $\alpha=15°$ and 45° as a function of z, respectively. These figures give us a numerical estimation of the variation of density of different charge species along z. Since the discharge is not uniform along the edges of the electrons, variations of charge densities in Figs. 5(a) and 5(b) are not the same.

Figure 6 shows the spatial distribution of vectors of the time average of electrodynamic force $\mathbf{F}=e(n_{O_2^+}-n_e-n_{O^-})\mathbf{E}$ for pulsed dc plasma actuator. The force is strong close to the common edges of dielectric and electrodes due to high electric field and ionization. The direction of time averaged force is in positive z-direction from the powered electrode to grounded electrode (from anode to cathode). This may be

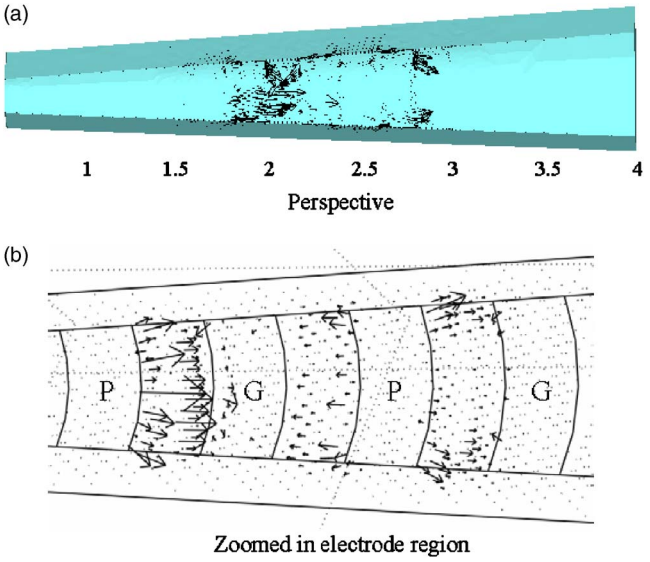

FIG. 6. (Color online) Vectors of electrodynamic force $\mathbf{F}=e(n_{O_2^+}-n_e-n_{O^-})\mathbf{E}$: (a) perspective and (b) zoomed in the electrode region.

useful in separation control. The solution will be sensitive to the initial conditions; we have taken only one initial condition which is close to the atmospheric condition. We have investigated the role of negative oxygen ions O_2^- in air chemistry and found that the density of negative oxygen ions O_2^- remains lower than that of positive oxygen ions O_2^+. The positive oxygen ions O_2^+ play more important role compared to O_2^-. These results will be described in another forthcoming study.

V. CONCLUSIONS

We have studied a pulsed dc plasma actuator operating in oxygen using a self-consistent multibody modeling of oxygen, plasma, and dielectric. The chemistry of formation of different species of oxygen has been taken into account. Species with very high recombination rates and nitrous oxide have been neglected for simplicity. Continuity equations governing densities of electrons, ions, and neutral species of nitrogen and oxygen are solved with Poisson's equation using a three-dimensional finite element based formulation of plasma to obtain spatial and temporal profiles of densities of species and electric field. The electric field and ionization are highest close to the common edges of electrodes and dielectric. Oppositely charged species move in opposite directions due to the applied pulsed dc potential which gives rise to charge separation. Poisson's equation governs the electric field generated due to charge separation. The density of the separated charge $n_q=(n_{O_2^+}-n_e-n_{O^-})$ and the electrodynamic force per volume $\mathbf{F}=e(n_{O_2^+}-n_e-n_{O^-})\mathbf{E}$ have been obtained. Numerical predictions show a dc corona type plasma instability similar to experimental observations. The time average of the force shows mostly acceleration in the forward direction (from anode to cathode) above the actuator. This results in a moving wave of plasma over the surface in forward direction which can find application in flow control. A pulsed dc plasma actuator may be used as an alternative to the dielectric barrier discharge plasma actuator.

ACKNOWLEDGMENTS

This work was partially supported by the AFOSR Grant Nos. FA9550-07-1-0131 and FA9550-05-1-0074 monitored by Dr. John Schmisseur and LtCol Rhett Jefferies and AFRL research fellowships during the past summers. The authors acknowledge thoughtful discussions with Dr. Datta Gaitonde and Dr. Miguel Visbal.

[1]J. R. Roth, D. M. Sherman, and S. R. Wilkinson, AIAA J. **38**, 7 (2000).
[2]C. L. Enloe, T. E. McLaughlin, G. I. Font, and J. W. Baughn, *Proceedings of the 44th AIAA Aerospace Sciences Meeting and Exhibit, Reno, Nevada, 9–12 January 2006* (AIAA, Washington, D.C. 2002), Paper No. AIAA 2006-166.
[3]S. Roy and D. V. Gaitonde, *Proceedings of the 43rd AIAA Aeropsace Sciences Meeting, Reno NV, 10–13 January 2005* (AIAA, Washington, DC, 2002), Paper No. AIAA-2005-0160.
[4]S. Roy, K. P. Singh, and D. V. Gaitonde, Appl. Phys. Lett. **88**, 121501 (2006).
[5]J. Poggie, *Proceedings of the 36th AIAA Plasmadynamics and Lasers Conference, Toronto, Ontario, Canada, 6–9 June 2005* (AIAA, Washington, DC, 2002), Paper No. AIAA 2005-5303.
[6]K. P. Singh and S. Roy, J. Appl. Phys. **101**, 123308 (2007).
[7]B. Jayaraman, S. Thakur, and W. Shyy, J. Heat Transfer **129**, 517 (2007).
[8]A. V. Likhanskii, M. N. Shneider, S. O. Macheret, and R. B. Miles, Phys. Plasmas **14**, 073501 (2007).
[9]T. C. Corke, M. L. Post, and D. M. Orlov, Prog. Aerosp. Sci. **43**, 193 (2007).
[10]G. I. Font, C. L. Enloe, T. E. McLaughlin, and D. Orlov, *Proceedings of the 45th AIAA Aerospace Sciences Meeting and Exhibit, Reno, Nevada 2007* (AIAA, Washington, DC, 2002), Paper No. AIAA 2007-188.
[11]J. W. Gregory, C. L. Enloe, G. I. Font, and T. E. McLaughlin, *Proceedings of the 45th AIAA Aerospace Sciences Meeting and Exhibit, Reno, Nevada 2007* (AIAA, Washington, DC, 2002), Paper No. AIAA 2007-185.
[12]S. Pavon, J.-L. Dorier, Ch. Hollenstein, P. Ott, and P. Leyland, J. Phys. D **40**, 1733 (2007).
[13]C. O. Porter, J. W. Baughn, T. E. McLaughlin, C. L. Enloe, and G. I. Font, *Proceedings of the 44th AIAA Aerospace Sciences Meeting and Exhibit, Reno, Nevada, 9–12 January 2006* (AIAA, Washington, DC, 2002), Paper No. AIAA 2006-104.
[14]K. P. Singh and S. Roy, J. Appl. Phys. **103**, 013305 (2008).
[15]M. P. Patel, T. T. Ng, S. Vasudevan, T. C. Corke, M. L. Post, T. E. McLaughlin, and C. F. Suchomel, *Proceedings of the 45th AIAA Aerospace Sciences Meeting and Exhibit, Reno, NV, 8–11 January 2007* (AIAA, Washington, DC, 2002), Paper No. AIAA 2007-635.
[16]T. C. Corke, B. Mertz, and M. P. Patel, *Proceedings of the 44th AIAA Aerospace Sciences Meeting and Exhibit, Reno, Nevada, 9–12 January 2006* (AIAA, Washington, D.C. 2002), Paper No. AIAA 2006-1208.
[17]K. P. Singh and S. Roy, Appl. Phys. Lett. **91**, 081504 (2007).
[18]J. R. Roth and X. Dai, *Proceedings of the 44th AIAA Aerospace Sciences Meeting and Exhibit, Reno, Nevada, 9–12 January 2006* (AIAA, Washington, DC, 2002), Paper No. AIAA 2006-1203.
[19]O. A. S. Kandil, H. Hazem, and C. H. Liu, *Proceedings of the AIAA Atmospheric Flight Mechanics Conference, Hilton Head Island* (SC, Washington, 1992), Paper No. AIAA 1992-244.
[20]B. Jayaraman and W. Shyy, Prog. Aerosp. Sci. **44**, 139 (2008).
[21]Z. Z. Celik and L. Roberts, *Proceedings of the AIAA Atmospheric Flight Mechanics Conference, Hilton Head Island* (SC, Washington, 1992), Paper No. AIAA 1992-293.
[22]N. Pedreiro, S. M. Rock, Z. Z. Celik, and L. Roberts, J. Aircr. **35**, 69 (1998).
[23]V. Shalaev, A. Fedorov, N. Malmuth, V. Zharov, and Ivan Shalaev, *Proceedings of the 41st Aerospace Sciences Meeting and Exhibit, Reno, Nevada, 6–9 January 2003* (AIAA, Washington, DC, 2002), Paper No. AIAA 2003-34.
[24]A. A. Maslov, B. Y. Zanin, A. A. Sidorenko, B. V. Postnikov, V. P. Fomichev, A. D. Budovsky, and N. Malmuth, *Proceedings of the 43rd AIAA Aerospace Sciences Meeting and Exhibit, Reno, Nevada, 2005* (AIAA, Washington, DC, 2002), Paper No. AIAA-2005-400.
[25]K. P. Singh and S. Roy, J. Appl. Phys. **101**, 093301 (2007).
[26]I. A. Kossyi, A. Yu Kostinsky, A. A. Matveyev, and V. P. Silakov, Plasma Sources Sci. Technol. **1**, 207 (1992).
[27]S. Roy and B. P. Pandey, Phys. Plasmas **9**, 4052 (2002).
[28]H. W. Ellis, R. Y. Pai, E. W. McDaniel, E. A. Mason, and L. A. Viehland, At. Data Nucl. Data Tables **17**, 177 (1976).